^{181}Ta(n,γ) cross section and average resonance parameter measurements in the unresolved resonance region from 24 to 1180 keV using a filtered-beam technique

B. J. McDermott,* E. Blain, A. Daskalakis, N. Thompson, A. Youmans, H. J. Choun, W. Steinberger, and Y. Danon†
Rensselaer Polytechnic Institute, Gaerttner LINAC Center, 110 8th Street, Troy, New York 12180, USA

D. P. Barry, R. C. Block, B. E. Epping, G. Leinweber, and M. R. Rapp
Naval Nuclear Laboratory P.O. Box 1072, Schenectady, New York 12301-1072, USA
(Received 19 April 2017; published 13 July 2017)

A new array of four Deuterated Benzene (C_6D_6) detectors has been installed at the Gaerttner Linear Accelerator Center at Rensselaer Polytechnic Institute for the purpose of measuring neutron capture cross sections in the keV region. Measurements were performed on samples of ^{181}Ta in the unresolved resonance region (URR) using a filtered-beam technique, by which a 30 cm iron filter was placed in a white-spectrum neutron beam to remove all time-dependent γ-ray background and all neutrons except those transmitted through resonance-potential interference "windows" in the iron. The resulting filtered beam was effectively a quasimonoenergetic neutron source, which was used for performing measurements on isotopes with narrow level spacings in the URR. The capture cross-section results obtained for two thicknesses of tantalum are in agreement with those documented in the JEFF-3.2 library, as are the average resonance parameters obtained via a fit to the data using the SAMMY-FITACS code.

DOI: 10.1103/PhysRevC.96.014607

I. INTRODUCTION & BACKGROUND

A. Motivation

Advances in modern computing have enabled fast and efficient simulation of neutron transport problems for a wide variety of applications. The validity of these computations, however, is ultimately constrained by the accuracy, completeness, and quality of the evaluated nuclear cross-section data they incorporate.

New generations of fast-spectrum reactors and reactors proposed for space applications have considered the use of tantalum ($Z = 73$) and its alloys as both a reactivity control and structural material [1], because its high melting point and corrosion resistance make it an attractive choice for these high power density applications [2]. Earlier critical benchmark experiments have revealed 7–9% discrepancies in the predicted and measured critical masses for harder-spectrum, graphite-moderated, tantalum-reflected assemblies [3,4], indicating a need for additional differential cross-section measurements in the keV region. Comparisons of the ENDF/B-VII.1, JEFF-3.2, and JENDL-4.0 evaluated data libraries also exhibit notable discrepancies in both the (n, tot) and (n,γ) cross sections for ^{181}Ta at these energies (Fig. 1).

B. Cross-section measurements

Differential neutron cross-section measurements are typically performed using a pulsed neutron source with a "white," or continuous, energy spectrum. The sample and detection system are located some distance L from the neutron source. The elapsed time between the time of the neutron pulse and the detection of an event (t) is known as the time of flight (TOF) and is used to determine the energy of the incident neutrons (E_n). For a nonrelativistic case ($E_n \lessapprox 2$ MeV), TOF can be converted to energy through the familiar expression for kinetic energy

$$E_n = \frac{1}{2} m_n \left(\frac{L}{t - t_0}\right)^2 = \left(\frac{KL}{t - t_0}\right)^2, \tag{1}$$

where L is the flight path length in meters, t and t_0 are in μs, and $K = 72.29824 \frac{\mu s\sqrt{eV}}{m}$. The t_0 term accounts for the slight electronic delay that occurs between the start of the TOF clock sweep and the actual time of the neutron burst.

For a capture sample and detector located at a flight path of L, the count rate in the detector as a function of TOF, t, is given by

$$\dot{C}(t) = A\eta_c \phi(t) Y(t) + \dot{B}(t) + \dot{B}_0, \tag{2}$$

where A is the area of the sample in the neutron beam, η_c is the detection efficiency for a capture event, $\phi(t)$ is the neutron flux incident on the sample, and $Y(t)$ is the experimental capture yield or the probability that an incident neutron will undergo capture in the sample. The time-dependent background rate attributable primarily to in-beam photons (and some scattered neutrons) is given by $\dot{B}(t)$, and the ambient, time-independent background is denoted by $\dot{B}_0$.

The quantity of interest, the energy-dependent capture yield, is denoted by $Y_\gamma(E_n)$ and is given by

$$Y_\gamma(E_n) = \frac{\sigma_\gamma(E_n)}{\sigma_t(E_n)}(1 - e^{-N\sigma_t(E_n)}) + Y_m, \tag{3}$$

where Y_m is the capture yield for neutrons that undergo one or more scattering reactions prior to capture. The yield for neutrons that are captured on the first interaction is given by the first term of Eq. (3), and is termed the *primary yield*.

*brianj.mcdermott@unnpp.gov
†danony@rpi.edu

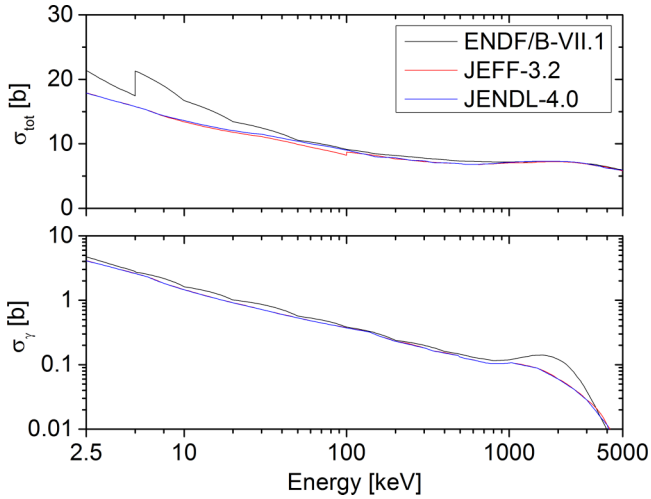

FIG. 1. ^{181}Ta (n,tot) and (n,γ) cross-section evaluations. ENDF/B-VII.1 exhibits significant anomalies compared to the other libraries [5].

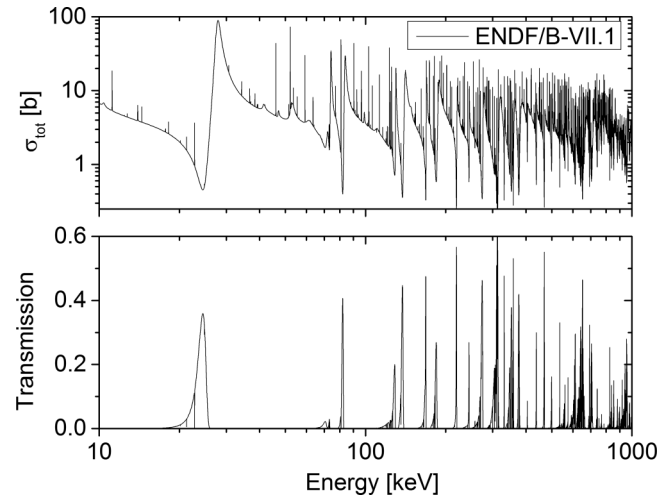

FIG. 2. Total ENDF/B-VII.1 cross section of elemental iron compared with energy-dependent neutron transmission through a 30 cm iron slab [5,9].

The experimental yield contains both the primary and multiply-scattered capture yields, as well as a number of secondary effects as illustrated in Eq. (4) [6].

$$Y_{\mathrm{expt}}(t) = f_n \int R_t(t,E_n)[(k_a(\sigma_T)\eta_\gamma(E_n)Y_\gamma(E_n) + \eta_n(E_n)Y_n(E_n)]\,dE_n. \quad (4)$$

In Eq. (4), f_n is a normalization constant, and R_t is a neutron energy resolution broadening function inherent in the TOF spectrometer setup. $Y_\gamma(E_n)$ is modified by the resolution function, as well as the detector's photon detection efficiency η_γ and a factor k_a, which is dependent on the total cross section of the sample and accounts for the effective reduction in detection efficiency due to the attenuation of capture photons as they traverse the thickness of the sample [6]. A second yield term $Y_n(E_n)$ and its associated efficiency $\eta_n(E_n)$ are added to account for neutrons that undergo scattering reactions in the sample and are subsequently captured in nearby materials, inducing a false capture signal in the detector system. It is thus the goal of the experimenter to isolate the primary yield by reducing the other secondary effects in Eq. (4) as much as possible when designing the measurement, and to correct for them when they cannot be reasonably reduced any farther.

White-spectrum neutron beams used in TOF experiments are accompanied by time-varying photon and neutron background resulting from secondary photon-emitting neutron interactions occurring further upstream in the beam. While a number of techniques exist for determining and correcting for this background contribution [1,5], there is ultimately an unavoidable amount of experimental uncertainty introduced when these corrections are applied. These methods [7] typically utilize strong, saturated resonances in filters that are introduced into the neutron beam, removing the primary beam in the resonance location leaving only the background. However, above a few tens of keV, very few such strong resonances are available, making background corrections subject to greater uncertainty. An alternative method introduced here using a filtered beam can be used instead to eliminate the in-beam background contribution completely, allowing higher accuracy measurements in the mid-to-upper keV region, as well as providing additional validation for more conventional background subtraction methods.

For average cross-section measurements in the unresolved resonance region (URR), on nuclides where the average nuclear level spacing $\langle D_\ell \rangle$ is narrow ($\lesssim$20 eV), a novel method of eliminating this time-dependent background is to introduce a thick iron filter into the beam path [8,9]. This filter attenuates all in-beam γ rays and nearly all neutrons except those whose energies fall within resonance potential interference "windows" in ^{56}Fe (Fig. 2). The neutrons that stream through the filter transmission windows provide, in effect, a quasimonoenergetic neutron beam. This method has been employed in a number of transmission and capture measurements on tantalum in the past, with a specific emphasis on the transmission window in iron at $\approx$24 keV [8,10]. However, as apparent in Fig. 2, iron possesses many filter windows from 24 keV to 1 MeV, presenting an opportunity for pointwise average cross-section measurements in this region with better signal-to-background ratios and statistical accuracy than conventional, unfiltered measurements.

Since the width of each filter window is on the order of a few keV, this method is best suited for isotopes with level spacings narrower than 20–30 eV, such that a large enough number of resonance levels are included in the averaging interval to reduce the observed fluctuations in the cross section. Tantalum, with a level spacing of 4.12 eV [11], is thus a good candidate for a filtered-beam experiment.

II. EXPERIMENTAL

A. Detectors

The experimental setup consists of four Deuterated Benzene (C_6D_6) [where D denotes deuterium (^{2}H)] detector modules[1] that have been custom designed with thin-wall

[1]Manufactured by Eljen Technology, 1300 W. Broadway St., Sweetwater, TX, USA 79556.

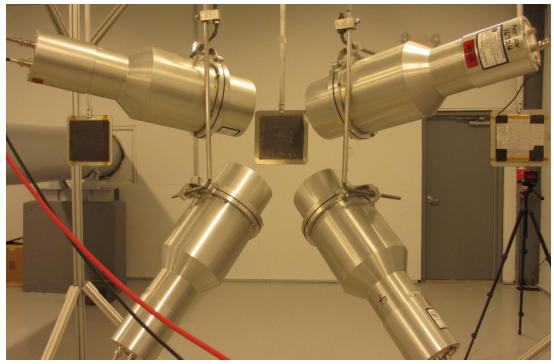

FIG. 3. The C_6D_6 detector system used in this work. The rectangular sample is positioned at the center of the four detector modules.

aluminum liquid scintillator cells and light shields, a thin μ-metal tape for magnetic shielding, as well as boron-free photomultiplier tube (PMT) windows, all of which are meant to minimize detector sensitivity to scattered neutrons [12]. The detector modules are mounted to a lightweight aluminum support structure, which is similarly intended to minimize neutron sensitivity. The modules are also placed on a 125° back angle with respect to the neutron beam to remove any potential biases due to anisotropies in the capture cascade [6,13]. The full setup is pictured in Fig. 3.

Data acquisition is handled using an SIS-3305 digitizer module,[2] with a 10-bit analog-to-digital converter (ADC) resolution and a 1.25 GHz sampling rate. Pulses from each detector are digitized and saved to disk for later off-line processing and analysis.

Detection systems for measuring capture cross sections require that the efficiency to detect a capture event be independent of the γ-cascade pathway. The C_6D_6 detectors satisfy this criterion by applying the total-energy detection principle [14] in conjunction with the pulse-height weighting technique [15]. In this arrangement, the detection system relies on low intrinsic efficiency to register only a single γ-ray per capture event. It is also asserted that the detection efficiency for an individual γ ray (η_γ) be proportional to its incident energy E_γ:

$$\eta_\gamma = kE_\gamma. \tag{5}$$

In the most general case, the efficiency to detect a capture event, η_c, is related to the detection efficiencies of the individual photons in the cascade by the relation

$$\eta_c = 1 - \prod_{i=1}^{m_\gamma}(1-\eta_{\gamma,i}), \tag{6}$$

where m_γ is the cascade multiplicity. If the individual photon detection efficiency is low (i.e., $\eta_{\gamma,i} \ll 1$), the detection efficiency for the full capture event can be approximated by

$$\eta_c \approx \sum_{i=1}^{m_\gamma}\eta_{\gamma,i}. \tag{7}$$

Via Eqs. (5) and (7), it can now be shown via Eq. (8) that the efficiency to detect a capture event is directly proportional to the total excitation energy of the compound nucleus, and thus insensitive to the cascade pathway:

$$\eta_c \approx k\sum_{i=1}^{m_\gamma}E_{\gamma,i} \approx kE_x = k(S_n + E_n). \tag{8}$$

With few exceptions [14], the photon detection efficiency is rarely proportional to incident photon energy. In order to satisfy the proportionality requirement, a weighting function is applied to the detector response function.

Photons incident on a detector with energy E_γ deposit a certain amount of energy E_d within the detection volume. The distribution of E_d given a certain E_γ is the detector response function $R(E_d,E_\gamma)$. For an organic scintillator like C_6D_6, Compton scatterings comprise the majority of photon interactions taking place within the detection volume. Thus, the energy deposition distribution takes on the characteristic shape of a Compton-continuum spectrum. Integrating this response function with respect to E_d yields the total detection efficiency for a photon with energy E_γ:

$$\eta_\gamma = \int_0^\infty R(E_d,E_\gamma)\,dE_d. \tag{9}$$

In order to invoke the total energy method, the energy proportionality assertion in Eq. (5) is applied to Eq. (9) by modifying the detector's response function with a weighting function $W(E_d)$:

$$\eta_\gamma = kE_\gamma = \int_0^\infty R(E_d,E_\gamma)W(E_d)\,dE_d. \tag{10}$$

To determine the weighting function, a number of response functions must be generated *a priori* via MCNP-6.1 [16] simulations of photon transport through the sample, detector, and any nearby materials [6]. This requires a very detailed model of the experimental setup like the one shown in Fig. 4. In the simulation, monoenergetic photons were emitted isotropically from the sample, and F8 (pulse height) tallies were taken in each of the detector modules (Fig. 5). This was repeated for

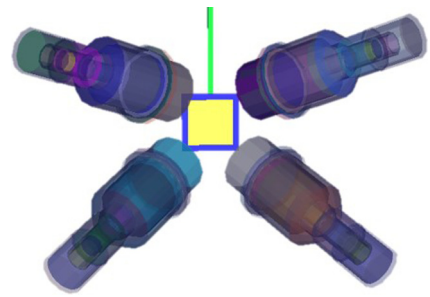

FIG. 4. 3D rendering of the MCNP geometry of the detector system and sample used in this work [5].

[2]Manufactured by Struck Innovative Systeme GmbH, Harksheider Str. 102A, 22399 Hamburg, Germany.

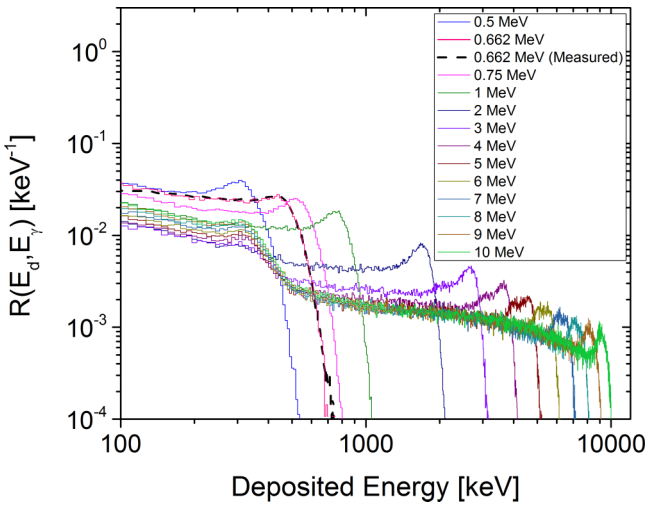

FIG. 5. Selection of MCNP-generated response functions used in weighting function fitting. The dotted line shows the measured response to a ^{137}Cs check source.

approximately 20 photon energies, as well as several different spatial distributions within the sample, as capture reactions tend to be surface-peaked in the vicinity of strong resonances. The F8 tally was resolution broadened using a Gaussian kernel derived from experimental measurements of the γ-ray spectra of ^{22}Na, ^{137}Cs, and ^{12}C* calibration sources [5].

The weighting function was then parametrized as a fifth-order polynomial, and a linear least-squares fit of the polynomial coefficients was performed to find the weighting function that best satisfied the proportionality requirement of Eq. (5). The overall effect of the weighting function is generally to more heavily weight higher energy photons for which the real efficiency would normally be low. This has the overall effect of removing any potential bias attributable to variations in the multiplicity and energy spectra of individual capture cascades.

B. Measurement methods

1. Sample properties

Two rectangular samples of 99.95% pure elemental tantalum were selected for measurement in two separate experimental campaigns. The minor isotope of tantalum, ^{180m}Ta, is present in a concentration of 120 ppm [17], which is on the same order as the concentration of other impurities in the samples. The contributions to the capture yield from both ^{180m}Ta and other impurities were thus assumed to be negligible.

Sample thicknesses of approximately 2 mm and 6 mm, were chosen to provide a high counting rate, and to provide a saturated resonance to which to normalize the filtered-beam data. The dimensions and number densities for each sample are tabulated in Table I. The impurity concentrations for each sample are tabulated in Table II.

A B_4C sample, enriched to 91.7% ^{10}B and having a nominal thickness of 1.30 cm [18], was used to provide a measurement of the energy-dependent flux shape via detection of the 478 keV photons emitted in ^{10}B(n,α_γ) reactions. A $10 \times 10 \times 1$ cm^3 sample of elemental lead was used to measure the time-dependent profile of the in-beam photon background in the unfiltered beam measurements, as described in Sec. III B.

TABLE I. Dimensions and number densities for the tantalum samples used in each measurement campaign.

	Run 1	Run 2
X (cm)	10.209 ± 0.001	10.430 ± 0.001
Y (cm)	10.205 ± 0.001	10.262 ± 0.001
Z (cm)	0.202 ± 0.001	0.641 ± 0.001
N (atm/b)	0.0358 ± 0.0012	0.0112 ± 0.0009

Each sample was mounted to a 1.588 mm (1/16 in.) thick aluminum frame using 0.508 mm (0.020 in.) Kapton tape. The sample holder frames, in turn, were mounted to a Velmex BiSlide linear translation assembly, which employs a 0.001-in. resolution stepper motor to position the samples in the beam.

2. Measurement procedure

The experimental campaigns consisted of two, week-long measurement efforts at the Gaerttner Linear Accelerator Center at Rensselaer Polytechnic Institute (RPI LINAC). Each measurement was divided into two phases, one for performing the filtered-beam measurements and one for performing measurements with the filter removed for the purposes of black-resonance normalization and comparison with the filtered-beam method.

The filtered-beam runs were performed by placing a 30 cm slab of elemental iron in the path of the neutron beam [9]. A 5/32 in. thick B_4C filter was also placed in the beam to remove any low-energy "overlap" neutrons. The LINAC electron pulse width was set to a nominal value of 30 ns, and the pulse repetition rate was set to 400 Hz. During the unfiltered normalization runs, the pulse width was widened to 200–250 ns, and the pulse repetition rate was lowered to 250 Hz in order to achieve higher beam powers and longer energy rundowns needed to observe the tantalum resonances in the eV region. A ^{nat}Cd overlap filter was placed in the beam to remove overlap neutrons with energies lower than 0.5 eV. The LINAC pulse widths, which dominate the resolution broadening of the TOF spectrometer setup in this work [5], were determined at the time of the experiments by measuring the FWHM of the bremsstrahlung γ flash.

Samples were cycled in and out of the beam at regular intervals, with total measurement times summarized in Table III. Flux monitor counts were recorded during each sample measurement to account for fluctuations in the beam intensity over the course of the experiment. Measurements of the ambient background with the accelerator off were also performed before and after each set of measurements.

III. DATA REDUCTION

A. Pulse processing

A typical measurement campaign generates many tens to hundreds of gigabytes of digitized detector pulses. Using custom-developed software tools, the raw waveforms were

TABLE II. Tantalum sample impurities.

Impurity	Atom fraction (ppm)	
	Ta-2	Ta-6
Ag	<0.1	[a]
Al	0.041	[a]
As	<0.05	[a]
B	<0.01	[a]
Be	<0.01	[a]
Bi	<0.01	[a]
C	6	30
Ca	<0.05	[a]
Cd	<0.1	[a]
Cl	0.081	[a]
Co	<0.005	[a]
Cr	0.012	[a]
Cu	0.044	[a]
Fe	0.027	<1
H	2	5
In	<0.05	[a]
K	0.057	[a]
Li	<0.01	[a]
Mg	<0.01	[a]
Mn	<0.01	[a]
Mo	14	6
N	18	[a]
Na	<0.012	[a]
Nb	1000	72
Ni	0.005	<1
O	48	92
P	0.025	[a]
Pb	<0.03	[a]
S	0.019	[a]
Sb	<0.1	[a]
Si	0.041	<1
Sn	<0.1	[a]
Th	0.008	[a]
Ti	0.024	<1
U	<0.005	[a]
V	0.002	[a]
W	70	36
Zn	<0.05	[a]
Zr	0.4	[a]

[a]Not reported by supplier.

TABLE III. Sample run times.

Sample	Total triggers		Total time (hr)	
	Filtered	Unfiltered	Filtered	Unfiltered
Ta-2	37344061	4394231	25.93	4.88
Ta-6	14556121	2425698	10.11	2.70
$^{10}B_4C$	18238973	6956924	12.67	4.83
^{nat}Pb	4063571	606076	2.82	0.67
Open beam		4310474		2.99

reconstructed, and the relevant parameters, such as pulse integral and time of flight, were extracted.

To invoke the weighting function, it was necessary to determine the deposited energy E_d for each recorded pulse. To achieve this, the integral of a detector pulse, I_{ADC}, was first determined by summing up the digitized values of each time step of the waveform. I_{ADC} was then converted to the deposited energy E_d by a linear calibration curve determined during the pre-experiment setup using ^{22}Na and ^{137}Cs calibration sources. This curve is given by

$$E_d = a I_{\mathrm{ADC}} + b. \tag{11}$$

The value obtained for E_d was then used to determine the weight for that detector event. For construction of the TOF histogram, the channel corresponding to E_d was incremented by the calculated weight. The extracted event parameters were saved and stored in an HDF5-formatted file [19], where they could be rapidly queried and re-analyzed with different weighting, filtering, and binning schemes as deemed appropriate.

B. Capture yield determination

1. Filtered

The raw count rate data from the filtered-beam data are shown in Fig. 6. The filter windows are visible as prominent peaks in the counting rate in both the tantalum and B_4C samples, which rise above a flat, ambient background. The lead sample, a pure neutron and photon scatterer, shows no visible peaks in the regions of the filter windows, indicating that the filter has reduced the in-beam photon background to negligible levels, and that the detector system is insensitive to the effects of scattered neutrons.

In the filtered measurement, the reaction rate in the sample at each filter window is modified by the energy-dependent transmission through the filter. Because the $^{10}B(n,\alpha\gamma)$ cross

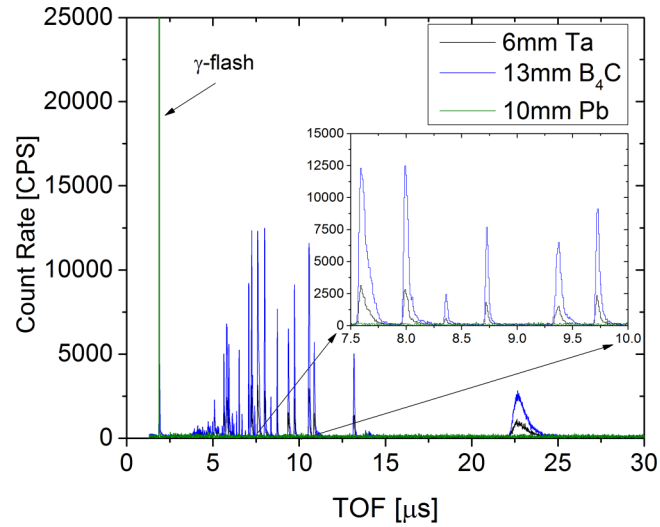

FIG. 6. Raw TOF spectra of filtered-beam measurements. Counts in both B_4C and Ta are observed at the Fe-transmission windows, and only ambient background is observed between the windows [5].

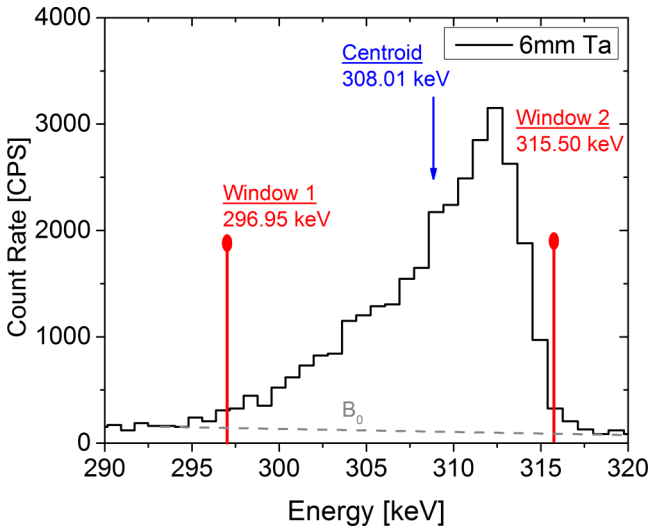

FIG. 7. Filter window at 308 keV in the Ta-6 sample measurement. The lower and upper energy limits, as well as the centroid energy, are shown.

section is standardized to 1% accuracy or better from thermal energies up to 1 MeV [20], the yield for this reaction, Y_B, is determined via MCNP calculation, and used as the cross-section reference in determining the energy-dependent shape of the neutron flux.

The background for each filter window was determined by finding the average counts in a selected range of channels on either side of a peak, then fitting a background line, B_0, between the regions, which is then subtracted from the peak (Fig. 7). The window limits on either side of the peak were selected using an algorithm that minimized the statistical uncertainty in the background-corrected integral counts in the peak [5,9].

The experimental yield in the sample, averaged over the width of the filter window, is given by Eq. (12), where C^{Ta} and C^{B} are the weighted, background-corrected counts in the filter windows (summed over all window channels) for the tantalum and B_4C samples, respectively. For these measurements, the count rate was low enough such that dead time was negligible (<0.1%). $\eta_\gamma^{\mathrm{Ta}}$ and η_γ^{B} are the average detection efficiencies for tantalum and ^{10}B photons. The monitor counts are denoted M^{Ta} and M^{B} for the tantalum and B_4C samples, respectively.

$$\bar{Y}^{\mathrm{Ta}}_{\mathrm{expt}} = \frac{\eta_\gamma^{\mathrm{B}}}{\eta_\gamma^{\mathrm{Ta}}}\frac{C^{\mathrm{Ta}}}{C^{\mathrm{B}}}Y^{\mathrm{B}}\frac{M^{\mathrm{B}}}{M^{\mathrm{Ta}}} = f_n\frac{C^{\mathrm{Ta}}}{C^{\mathrm{B}}}Y^{\mathrm{B}}\frac{M^{\mathrm{B}}}{M^{\mathrm{Ta}}}, \tag{12}$$

where the normalization factor f_n is defined as

$$f_n = \frac{\eta_\gamma^{\mathrm{B}}}{\eta_\gamma^{\mathrm{Ta}}}. \tag{13}$$

It is assumed that η_γ^{B} and $\eta_\gamma^{\mathrm{Ta}}$ are functions of the sample-detector geometry and the γ-cascade properties. It is further assumed that energy-dependent differences in the cascade multiplicity and energy spectrum are negligible.

The statistical uncertainty in the yield is given by

$$\frac{\Delta Y_{\mathrm{expt}}}{Y_{\mathrm{expt}}} = \sqrt{\left(\frac{\Delta C^{\mathrm{Ta}}}{C^{\mathrm{Ta}}}\right)^2 + \left(\frac{\Delta C^{\mathrm{B}}}{C^{\mathrm{B}}}\right)^2}, \tag{14}$$

where ΔC^{Ta} and ΔC^{B} are the uncertainties of the unweighted, background-corrected counts for the capture sample and B_4C sample, respectively. Because the number of monitor counts accumulated in each sample cycle is very large (>100 000), the statistical uncertainty attributable to the monitors is assumed to be negligible.

Other sources of uncertainty include the accuracy of the ^{10}B yield found in Ref. [20] (<1%), the accuracy of the weighting function (≈3%) [5], and the uncertainty in the normalization factor f_n, assumed to be attributable to counting statistics in the region of the black resonance used for normalization (1%).

2. *Unfiltered*

In a conventional unfiltered measurement, there is a time-dependent background component that results from the Compton scattering of photons in the beam into the detector modules. Because this background component is only present when a sample is present in the beam, simply subtracting measurements of the open beam alone are not adequate to account for the total time-dependent background.

One method to determine the time-dependent background component is to perform a measurement on a sample with a negligible capture cross section, such as lead. Assuming the sensitivity to scattered neutrons is also negligible, the signal in the detector will be nearly entirely due to the in-beam photon background. The lead sample acts, in effect, as a proxy for the time-dependent background shape.

The in-beam photon background consists primarily of 2.2 MeV γ rays resulting from neutron capture in the aqueous moderator of the LINAC target, and 1.5–2 MeV photons resulting from the decay of excited states in the tantalum target [5]. To properly normalize the background counts obtained with the lead proxy sample, Monte Carlo code MCNP simulations of the scattering probability of 2 MeV photons from Pb and Ta were performed, and F8 tallies of the pulse-height spectrum were taken in each of the detector modules. The ratio k_p of the integrated, weighted F8 spectra of the main tantalum sample and the lead sample was then used as a scaling factor by which the lead counting data were multiplied to obtain the magnitude of the in-beam background [Eq. (15)], shown for the 2 mm tantalum sample in Fig. 8.

$$k_p(E_\gamma) = \frac{A_{\mathrm{Pb}}}{A_{\mathrm{Ta}}}\frac{\int_{E_L}^{\infty} W_{\mathrm{Ta}}(E_d)R_{\mathrm{Ta}}(E_d,E_\gamma)\,dE_d}{\int_{E_L}^{\infty} W_{\mathrm{Pb}}(E_d)R_{\mathrm{Pb}}(E_d,E_\gamma)\,dE_d}. \tag{15}$$

The terms A_{Pb} and A_{Ta} in Eq. (15) refer to the areas of the lead and tantalum samples, respectively.

C. Normalization

A standard capture cross section or yield value must be known *a priori* in order to properly normalize the filtered-beam data. The most straightforward approach is to perform a short auxiliary measurement with the iron filter removed, and to

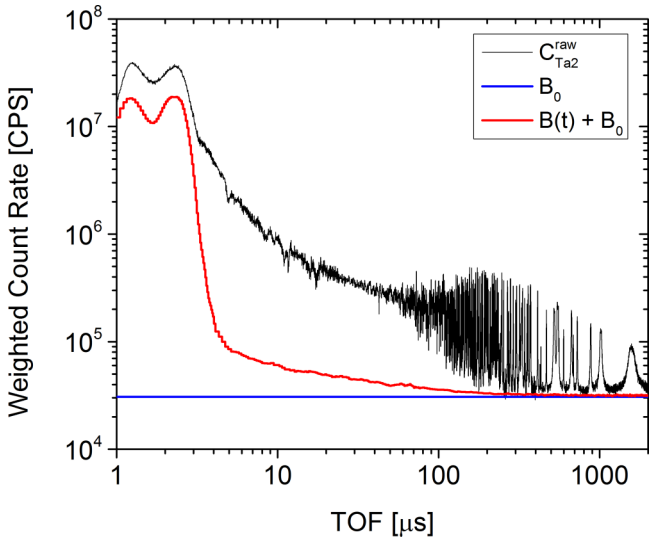

FIG. 8. Count rates for the 2 mm tantalum sample, the ambient background, and the in-beam background as a function of TOF [5].

use a saturated, capture-dominated resonance to determine the normalization coefficient. In the case of an unfiltered measurement, there exist a number of resonances in tantalum, the 4.28 eV resonance in particular, where $N\sigma_t \gg 1$, and thus $Y_c \approx 1$. Similarly, the experimental photon-production yield of the ^{10}B(n,α_1) reaction used in the flux-shape measurement approaches unity at this energy. Figure 9 compares the normalized, background-corrected count rate data in both the 2 mm tantalum and the B_4C sample. The yield in the saturated region of the 4.28 eV resonance matches the yield in the B_4C sample in the outlined region. The normalization factor f_n is given by

$$f_n = \frac{Y_{\gamma,\mathrm{Ta}}}{Y_{\gamma,\mathrm{B_4C}}} \frac{\dot{C}_{\mathrm{B_4C}} - \dot{C}_{\mathrm{bkg}}}{\dot{C}_{\mathrm{Ta}} - \dot{C}_{\mathrm{bkg}}}, \tag{16}$$

where $\dot{C}_{\mathrm{Ta}}$, $\dot{C}_{\mathrm{B_4C}}$, and $\dot{C}_{\mathrm{bkg}}$ are the count rates for tantalum, B_4C, and background, respectively. The resulting f_n value from the unfiltered measurement is then applied to the filtered-beam data to obtain the normalized capture yield for the filtered data points [Eq. (12)].

The strength of the 4.28 eV resonance is such that most of the capture events, and therefore photon production, in the saturated region occur at or near the surface of the sample. On the edges of the resonance, however, more capture events occur within the volume of the sample, and the subsequent cascade γ rays are subject to greater attenuation as they traverse the path through the sample to the detector. This overall effect leads to enhancement of the saturated region of the resonance and suppression of the edges.

A correction factor to account for this effect, k_a, was determined using a combination of Monte Carlo simulations performed with DICEBOX [21] and MCNP, and a subroutine was implemented in the SAMMY code in order to apply it to the calculated capture yield as a multiplier in the resolved resonance region [5]. The results of this correction factor are shown for each sample in Fig. 10, which compares the SAMMY default calculation to calculations performed using the k_a correction. The corrected SAMMY calculations show much better agreement with the data than the defaults, and were subsequently used to validate the normalization procedure.

The unfiltered data used to perform the normalization step were weighted with a weighting function modeled with the assumption that photon production was surfaced-peaked in the sample. The filtered-beam points, however, were measured

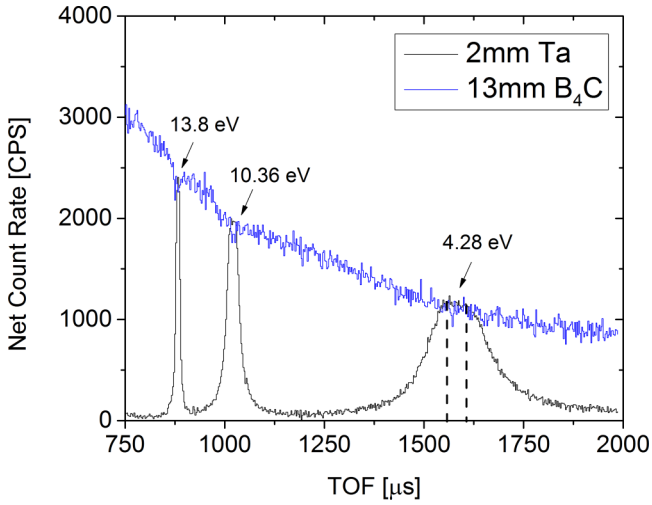

FIG. 9. Normalization of the ^{181}Ta saturated resonance at 4.28 eV to the B_4C measurement. Both measurements have $Y_{\mathrm{expt}} \approx 1$ in the outlined region [5]. The small depressions in the B_4C TOF spectrum in the vicinity of the tantalum resonances result from the partial removal of neutrons by the tantalum photoneutron target of the LINAC.

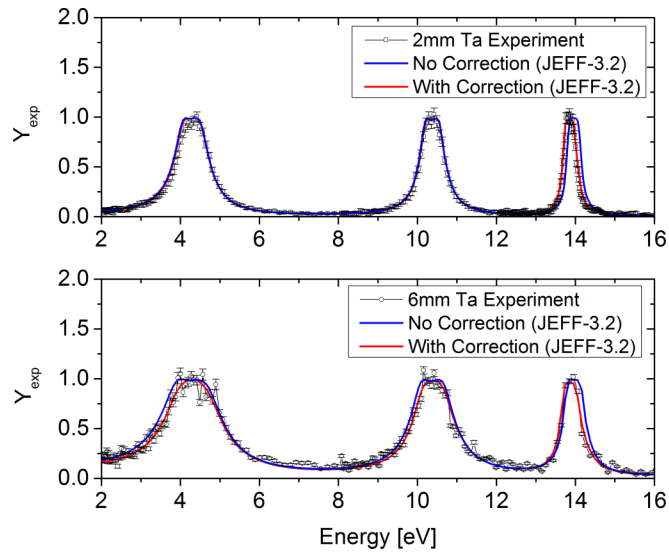

FIG. 10. Capture depth correction was implemented in SAMMY code to improve the calculation of the capture yield in thick, highly attenuating samples such as tantalum. The corrected yield exhibits closer agreement with the experimental data than the default SAMMY output.

in an energy region where the photon production was more uniform within the sample volume. To account for this difference, the normalization factor f_n was corrected by the ratio of the k_a value at the black resonance to the k_a value at the filter point. Similarly, the unfiltered data in the URR were corrected by multiplying f_n by k_a directly. This correction was not needed, however, for the $^{10}B_4C$ sample, because its low Z and density did not result in appreciable attenuation of its monoenergetic 478 keV photons.

D. Self-shielding and multiple scattering

In samples with non-negligible thickness, the measured yield is increased by neutrons that are captured after one or more initial scattering reactions within the sample. Resonance self-shielding is an effect that varies nonlinearly with sample thickness, and acts to depress the transmission of neutrons through the sample, thereby enhancing the observed capture yield. The non-negligible thickness of the tantalum samples used in this work requires corrections to be made for both resonance self-shielding and multiple scattering effects.

From the expression for primary capture yield [i.e., the first term of Eq. (3)], one can solve for σ_γ and perform a Taylor expansion about Y_γ to obtain the thin sample approximation for σ_γ:

$$\sigma_\gamma = \frac{Y_\gamma}{N}, \tag{17}$$

which is valid for the case of a thin sample in which multiple scattering and resonance self-shielding effects are negligible.

In a thick-sample case like that in this set of measurements, corrections to Eq. (17) are necessary in order to isolate the true capture cross section. These correction factors k_s were calculated using the SESH [22] and MCNP Monte Carlo codes [23]. The resulting correction factors are applied to the thin-sample approximation according to Eq. (18) to determine the capture cross section.

$$\sigma_\gamma = \frac{Y_\gamma}{k_s N}. \tag{18}$$

While SESH can only provide pointwise correction factors using relatively primitive geometries, it does not rely on *a priori* knowledge of the full cross-section data, as with MCNP. Instead, it only requires the input of the average resonance parameters S_ℓ, $\langle\Gamma_\gamma\rangle$, and $\langle D_0\rangle$. These parameters were taken from the *Atlas of Neutron Resonances* [11] for the initial calculation of k_s, and then from the resulting SAMMY-FITACS fits in Sec. IV B for subsequent iterations to verify convergence. The resulting correction factors from both MCNP and SESH calculations are shown in Fig. 11, the latter of which were used to perform the corrections in this work. The implication of the energy-dependent trend in k_s shown in Fig. 11 is that resonance self-shielding is the dominant effect below 10 keV, and multiple scattering dominates at higher energies.

E. Signal-to-background ratio

A major advantage of the filtered-beam method is the complete elimination of all beam-associated background

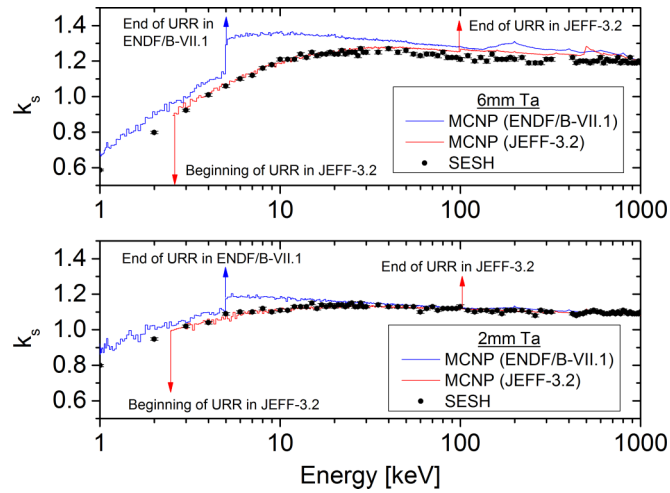

FIG. 11. Self-shielding and multiple scattering correction factors (k_s) for 2 and 6 mm tantalum samples were calculated using both MCNP and SESH. The simpler SESH results agree with the more detailed MCNP simulations.

in the measurement, leaving only the ambient component. Because the in-beam component becomes significant at TOFs corresponding to neutron energies above 100 keV, the filtered-beam method provides a way of better isolating the capture signal at these energies, without the need for corrections like those discussed in Sec. III B. Furthermore, this also provides additional, albeit indirect, verification and validation for those background corrections.

In the unfiltered measurements, the in-beam component represented a significant portion of the background above 1 keV, as shown in the signal to in-beam background plot in Fig. 12.

To directly compare the signal-to-background ratios of the filtered-beam measurements and the unfiltered measurements, it was necessary to normalize to the LINAC beam power, which was much higher for the unfiltered measurements. This was

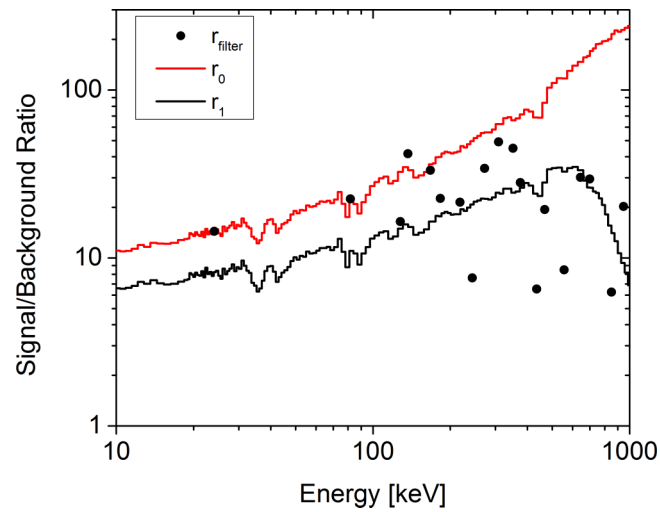

FIG. 12. Comparison of the signal-to-background ratio for the 2 mm tantalum sample in filtered and unfiltered configurations.

done finding the ratio k_f of the average energy deposited on the LINAC target per LINAC pulse:

$$k_f = \frac{f^{\text{filter}}}{f^{\text{unfilter}}} \frac{P_{\text{avg}}^{\text{unfilter}}}{P_{\text{avg}}^{\text{filter}}}, \tag{19}$$

where P_{avg} is the average LINAC power, and f is the pulse repetition rate.

The resulting signal-to-background ratios for the filtered and unfiltered measurements are plotted in Fig. 12. In the unfiltered measurement, the full signal-to-background ratio is given by

$$r_1(t) = \frac{\dot{C}(t) - \dot{B}(t) - \dot{B}_0}{\dot{B}(t) - \dot{B}_0}. \tag{20}$$

In the filtered measurement, however, the time-dependent background term is absent, and the signal-to-background ratio is given by

$$k_f \frac{\dot{C}(t) - \dot{B}_0}{\dot{B}_0}. \tag{21}$$

For the purposes of comparison, let us introduce the term r_0, which is the ratio of the time-dependent signal count rate in the unfiltered measurement, to the time-independent background:

$$r_0(t) = \frac{\dot{C}(t) - \dot{B}(t) - \dot{B}_0}{\dot{B}_0}. \tag{22}$$

Since the magnitude of the time-dependent background $\dot{B}(t)$ scales linearly with the LINAC beam intensity, increasing the beam power is subject to diminishing returns with regards to improving the signal-to-background ratio of an experiment. The filtered-beam method, however, is not subject to the same limitation due to the lack of beam-associated background, and the beam power can thus be increased arbitrarily without any corresponding increase in background. For points corresponding to the most prominent filter peaks, the signal-to-background ratio meets or exceeds r_1 of the unfiltered measurement, particularly at energies where in-beam background is a significant portion of the total signal. In the best case, the signal-to-background ratio approaches r_0, in which only the ambient background is the limiting factor.

IV. RESULTS AND ANALYSIS

A. Cross sections

Once the cross sections are obtained for each sample (for a total of n samples), a weighted average of all the samples' respective cross sections is then calculated to arrive at a single value [9]:

$$\bar{\sigma}_\gamma = \frac{\sum_1^n \frac{\sigma_{\gamma,i}}{(\Delta\sigma_{\gamma,i})^2}}{\sum_1^n \frac{1}{(\Delta\sigma_{\gamma,i})^2}}. \tag{23}$$

The uncertainty terms are taken to be the larger of either the internal statistical uncertainty of the data points or the external systematic uncertainty between the two measurements:

$$\Delta\sigma = \max(\Delta\sigma_{\text{internal}}, \Delta\sigma_{\text{external}}). \tag{24}$$

In this case, the internal error is given by [9]

$$\Delta\sigma_{\text{internal}} = \sqrt{\sum_1^n \frac{1}{(\Delta\sigma_i)^2}}, \tag{25}$$

and the external error is defined as [9]

$$\Delta\sigma_{\text{external}} = \sqrt{\frac{\sum_1^n \frac{(\bar{\sigma}-\sigma_i)^2}{(\Delta\sigma_i)^2}}{(n-1)\sum_1^n \frac{1}{(\Delta\sigma_i)^2}}}. \tag{26}$$

Finally, the average energy of each data point, E_c, was determined by finding the centroid of each transmission peak within the windowing limits c_1 and c_2 by weighting the energy

TABLE IV. Measured tantalum capture yields and cross sections with an iron-filtered beam.

Energy (keV)				Ta-2 mm				Ta-6 mm				Average	
E_c	E_1	E_2	ΔE	Y	$\Delta Y/Y$	σ_γ (b)	$\Delta\sigma_\gamma$ (b)	Y	$\Delta Y/Y$	σ_γ (b)	$\Delta\sigma_\gamma$ (b)	σ_γ (b)	$\Delta\sigma_\gamma$ (b)
23.654	20.999	25.991	3.361	0.0116	0.042	0.929	0.039	0.0419	0.045	0.947	0.042	0.937	0.029
81.592	79.977	82.697	2.359	0.00539	0.051	0.437	0.022	0.0198	0.051	0.450	0.023	0.443	0.016
127.82	125.88	129.63	3.416	0.00414	0.054	0.331	0.018	0.0156	0.058	0.362	0.021	0.346	0.014
136.85	134.51	138.65	3.973	0.00409	0.035	0.331	0.012	0.0150	0.039	0.351	0.014	0.340	0.0089
167.54	165.94	169.16	2.842	0.00389	0.049	0.314	0.016	0.0133	0.053	0.310	0.016	0.312	0.011
183.31	180.59	185.48	4.468	0.00365	0.051	0.299	0.015	0.0129	0.053	0.299	0.016	0.299	0.011
219.14	217.55	220.76	3.003	0.00310	0.063	0.257	0.016	0.0114	0.062	0.264	0.016	0.261	0.012
272.62	268.22	276.55	7.826	0.00287	0.040	0.237	0.0095	0.0104	0.044	0.247	0.011	0.242	0.0071
308.01	296.95	315.50	17.72	0.00268	0.033	0.221	0.0072	0.00978	0.037	0.228	0.0085	0.224	0.0055
351.59	343.57	360.73	16.80	0.00238	0.039	0.196	0.0077	0.00926	0.044	0.215	0.0094	0.205	0.0060
375.57	372.00	379.20	7.200	0.00232	0.052	0.190	0.0098	0.00818	0.054	0.190	0.010	0.190	0.0071
466.82	463.10	471.85	81.27	0.00219	0.071	0.177	0.013	0.00777	0.070	0.183	0.013	0.181	0.0090
554.94	550.12	561.46	9.390	0.00232	0.11	0.189	0.021	0.00765	0.14	0.180	0.025	0.186	0.016
643.51	619.95	664.18	44.23	0.00202	0.036	0.165	0.0059	0.00679	0.043	0.159	0.0068	0.163	0.0045
699.38	688.09	710.96	22.87	0.00177	0.053	0.145	0.0077	0.00682	0.055	0.161	0.0089	0.153	0.0058
946.98	929.22	968.97	36.73	0.00161	0.059	0.134	0.0079	0.00586	0.069	0.139	0.0096	0.136	0.0061
1181.2	1132.6	1227.8	78.14	0.00136	0.074	0.112	0.0083	0.00420	0.10	0.0998	0.010	0.108	0.0064

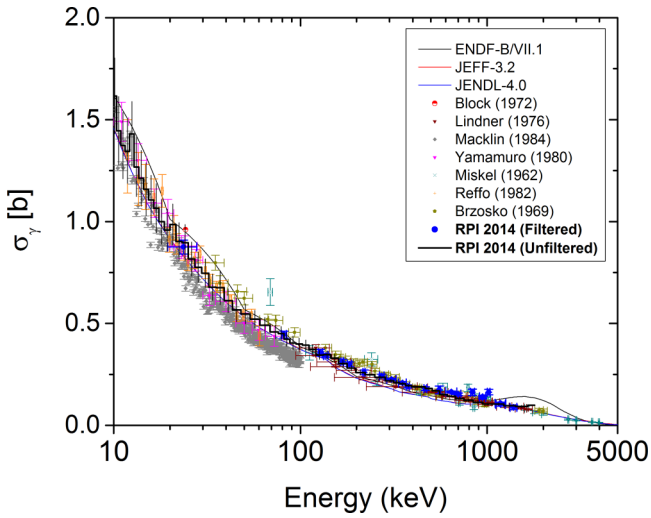

FIG. 13. Comparison of the experimental results of this work with past tantalum capture measurements and evaluations. Data are in excellent agreement with prior measurements [5].

points by the number of counts in each respective channel in the filter window [5,9]. To simplify the analysis, the same windowing limits were selected for both sample thicknesses. Points for which $r_{\text{filter}} < 10$ were excluded.

Seventeen data points were obtained from the filtered-beam measurement between 24 keV and 1 MeV and are listed in Table IV. The table lists the centroid energy E_c, lower and upper energy window limits E_1 and E_2, and energy span ΔE, as well as the yield Y, capture cross section σ_γ, and the uncertainties thereof. These points are also shown in Figs. 13 and 14, where they are compared with past experiments, present evaluated libraries, and the unfiltered measurements taken during this experiment. At higher energies, near 1 MeV, the apparent systematic differences between the filtered and unfiltered measurements are likely attributable to the small and irregularly-shaped filter peaks chosen at these points, which are

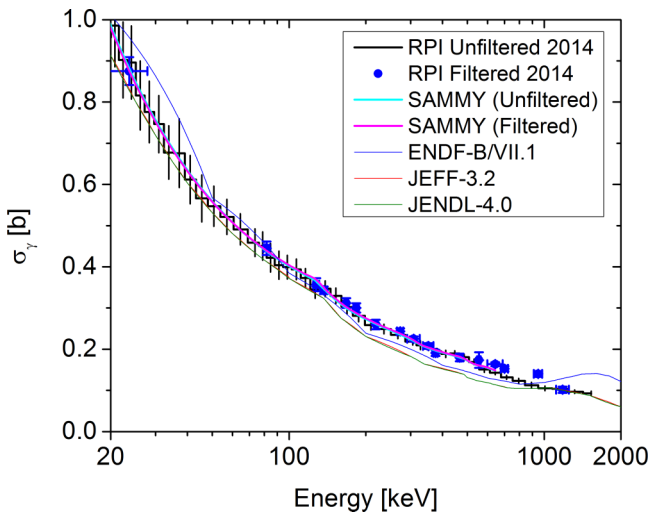

FIG. 14. Comparison of the experimental results of this work (and the corresponding SAMMY-FITACS fit) to existing evaluations.

TABLE V. ^{181}Ta strength functions.

$S_\ell \times 10^4$	Filtered	Unfiltered	JEFF-3.2	*Atlas* [11]
S_0	1.71 ± 0.12	1.70 ± 0.12	1.7	1.74 ± 0.12
S_1	0.52 ± 0.10	0.53 ± 0.09	0.3	0.5 ± 0.2
S_2	2.60 ± 0.60	2.45 ± 0.56	2.0	2.3 ± 0.3

less prominent and more affected by the ambient background than those at lower energies.

B. Average resonance parameters

From the cross-section data obtained in the previous section, average resonance parameters were fit to both filtered and unfiltered measurements from 20–600 keV using the FITACS code included in the SAMMY [24] analysis package. While SESH calculations indicate negligible amounts of resonance self-shielding (<1%) above 200 keV, the Hauser-Feshbach treatment of the cross section used by FITACS [24,25] was deemed appropriate for fitting at higher energies.

Fits were obtained for partial-wave strength functions S_ℓ, average radiation widths $\langle\Gamma_\gamma^\ell\rangle$, and distant level parameters R_ℓ^∞ and are summarized in Tables V–VII. For $\langle\Gamma_\gamma^\ell\rangle$ values where $\ell > 0$, the $\ell = 0$ value was used as the initial input to the solver. The input value of R^∞ was calculated from the effective potential scattering radius R', tabulated in [11] using the following expression [23]:

$$R^\infty = 1 - \frac{R'}{a_c}, \tag{27}$$

where a_c is the channel radius, given in units of fm by [23]

$$a_c = 1.23\left[\left(\frac{A}{m_n}\right)^{1/3} + 0.8\right]. \tag{28}$$

A and m_n are the atomic masses of the target nucleus and the neutron, respectively. The same value of R^∞ was used as the initial input for all values of ℓ.

The s-wave ($\ell = 0$) average level spacing $\langle D_0\rangle$ was fixed at the 4.17 eV value adopted in [11]. Because FITACS also requires total cross-section data to perform the fit, the JEFF-3.2 total cross section was input to the code in lieu of experimental total cross-section data.

Following the fit, the average resonance parameters were input back into SESH to perform another iteration of the self-shielding and multiple scattering correction. The calculated cross sections and resonance parameters on the second iteration did not differ from the original calculation by more

TABLE VI. ^{181}Ta Average radiation widths.

$\langle\Gamma_\gamma^\ell\rangle$ (meV)	Filtered	Unfiltered	JEFF-3.2	*Atlas* [11]
$\langle\Gamma_\gamma^0\rangle$	62.6 ± 5.1	63.4 ± 5.3	65	60.5 ± 2
$\langle\Gamma_\gamma^1\rangle$	55.0 ± 13.1	52.9 ± 13.5		
$\langle\Gamma_\gamma^2\rangle$	60.5[a]	60.5[a]		

[a]Not fitted.

TABLE VII. ^{181}Ta distant level parameters.

R_ℓ^∞	Filtered	Unfiltered	JEFF-3.2	*Atlas* [11]
R_0^∞	0.041 ± 0.020	0.042 ± 0.020		0.041 ± 0.20
R_1^∞	0.038 ± 0.019	0.036 ± 0.019		
R_2^∞	0.018 ± 0.011	0.017 ± 0.011		
R' (fm)	7.67 ± 0.080	7.66 ± 0.079		7.6 ± 0.2

than 0.3%, and thus no further iteration was necessary to achieve convergence.

The average resonance parameters obtained in the fit region compare well with the existing values of JEFF-3.2 and the *Atlas* to within experimental uncertainty. The current ENDF/B-VII.1 evaluation does not currently list average resonance parameters, but it is apparent that improvements are needed in its URR cross-section treatment above 3 keV.

V. CONCLUSION

The results of the set of measurements presented in Figs. 13 and 14 are largely consistent with the JEFF-3.2 and JENDL-4.0 evaluations below 100 keV. The filtered and unfiltered measurements are also consistent with one another, further validating the correction factors, normalization procedure, and time-dependent background subtraction methods. Comparisons of the experimental data with ENDF/B-VII.1 are problematic due to the anomalous interpolation features the evaluation exhibits above 3 keV. At higher energies, the capture contribution to the cross section is slightly higher than that presented in the JEFF and JENDL evaluations; however, there is strong consistency with the prior measurements shown in Fig. 13 all the way up to the measurement limit of 1.5 MeV. Above 1 MeV, the ENDF treatment of the cross section appears to be wholly inconsistent with the data obtained both in this work and in prior measurements. This is likely due to an incorrect theoretical treatment of the continuum region cross section, or contamination from inelastic scattering in the experimental datasets used when preparing the evaluation.

The advantages presented by the filtered-beam method are the complete removal of all time-dependent background and the subsequent improvements achieved in the overall signal-to-background ratio. The limiting factor is only the magnitude of the ambient background present in the experimental facility, and the relative intensity of the neutron beam. This makes it particularly attractive for future measurements to provide additional validation of keV-region capture cross sections and average resonance parameters of other nuclides with narrow level spacings, such as ^{197}Au, ^{232}Th, and ^{238}U.

ACKNOWLEDGMENTS

The authors extend their thanks to Peter Brand, Michael Bretti, Matthew Gray, Azeddine Kerdoun, and Larry Krusceski of the RPI LINAC technical team for their operation and maintenance of the accelerator facility during the course of this work. This work was performed under sponsorship of the U.S. Department of Energy Nuclear Criticality Safety Program.

[1] R. Macklin, Nucl. Sci. Eng. **86**, 362 (1984).
[2] T. Byoun, R. Block, and T. T. Semler, Tech. Rep. NASA-TM-X–69565, National Aeronautics and Space Administration (Government Printing Office, Washington, 1973).
[3] D. Loaiza, D. Gehman, R. Sanchez, D. Hayes, and M. Zerkle, Nucl. Sci. Eng. **160**, 217 (2008).
[4] M. Zerkle, M. Meyers, S. Tarves, and J. Powers, Tech. Rep. B-TM-1639, Bettis Atomic Power Laboratory, West Mifflin, PA 2006.
[5] B. McDermott, Ph.D. thesis, Rensselaer Polytechnic Institute, 2016.
[6] A. Borella, G. Aerts, F. Gunsing, M. Moxon, P. Schillebeeckx, and R. Wynants, Nucl. Instrum. Methods Phys. Res., Sect. A **577**, 626 (2007).
[7] R. Bahran, Ph.D. thesis, Rensselaer Polytechnic Institute, 2013.
[8] R. Block, N. Kaushal, and R. Hockenbury, in *Proceedings of the National Topical Meeting on New Developments in Reactor Physics* (American Nuclear Society, 1972), p. 1107.
[9] Y. Danon, R. Block, M. Rapp, F. Saglime, G. Leinweber, D. Barry, N. Drindak, and J. Hoole, Nucl. Sci. Eng. **161**, 321 (2009).
[10] N. Yamamuro, T. Doi, T. Miagawa, Y. Fujita, K. Kobayashi, and R. Block, J. Nucl. Sci. Technol. **15**, 637 (1978).
[11] S. Mughabghab, *Atlas of Neutron Resonances*, 5th ed. (Elsevier Science, New York, 2006).
[12] B. McDermott, R. Bahran, E. Blain, A. Daskalakis, S. Piela, and Y. Danon, in *Proceeding of the American Nuclear Society Student Conference, on CD ROM* (American Nuclear Society, 2013).
[13] B. McDermott, E. Blain, A. Daskalakis, N. Thompson, A. Youmans, H. Choun, W. Steinberger, Y. Danon, M. Rapp, G. Leinweber, D. Barry, B. Epping, and R. Block, in *Proceedings of the 2015 International Conference on Criticality Safety* (American Nuclear Society, 2015).
[14] M. Moxon and E. Rae, Nucl. Instrum. Methods **24**, 445 (1963).
[15] R. Macklin and J. Gibbons, Phys. Rev. **159**, 1007 (1967).
[16] The X-5 Monte Carlo Team, Monte Carlo Team, MCNP a general purpose Monte Carlo *N*-particle transport code, version 5, 2003.
[17] M. Weiser, N. Holden, T. Coplen, and J. Bohlke, Pure Appl. Chem. **85**, 1047 (2013).
[18] Z. Bartolome, Ph.D. thesis, Rensselaer Polytechnic Institute, 1968.
[19] The HDF Group, Hierarchical Data Format, version 5, 1997, accessed on Sept. 12, 2016.
[20] A. Carlson, V. Pronyaev, D. Smith, N. Larson, Z. Chen, G. Hale, and F. Hambsch, Nucl. Data. Sheets **110**, 3215 (2009).
[21] F. Bečvář, Nucl. Instrum. Methods Phys. Res., Sect. A **417**, 434 (1998).
[22] F. Frohner, Tech. Rep. GA-8380, Gulf General Atomic, Inc., San Diego, 1968.
[23] R. Bahran, D. Barry, R. Block, G. Leinweber, M. Rapp, A. Daskalakis, E. Blain, D. Williams, B. McDermott, L. Leal, and Y. Danon, Phys. Rev. C **92**, 024601 (2015).
[24] N. Larson, Tech. Rep. ORNL/TM-9179/R8, Oak Ridge National Laboratory, Oak Ridge, TN, 2008.
[25] W. Hauser and H. Feshbach, Phys. Rev. **87**, 366 (1952).